FULL PAPER

Imperfect spoiling in variable flip angle T_1 mapping at 7T: Quantifying and minimizing impact

Nadège Corbin ⓘ 🐦 | **Martina F. Callaghan** ⓘ 🐦

Wellcome Centre for Human Neuroimaging, UCL Queen Square Institute of Neurology, University College London, London, United Kingdom

Correspondence
Nadège Corbin, Wellcome Centre for Human Neuroimaging, UCL Queen Square Institute of Neurology, University College London, 12 Queen Square, London, WC1N 3AR, UK.
Email: n.corbin@ucl.ac.uk

Purpose: The variable flip angle (VFA) approach to T_1 mapping assumes perfectly spoiled transverse magnetisation at the end of each repetition time (TR). Despite radiofrequency (RF) and gradient spoiling, this condition is rarely met, leading to erroneous T_1 estimates (T_1^{app}). Theoretical corrections can be applied but make assumptions about tissue properties, for example, a global T_2 time. Here, we investigate the effect of imperfect spoiling at 7T and the interaction between the RF and gradient spoiling conditions, additionally accounting for diffusion. We provide guidance on the optimal approach to maximise the accuracy of the T_1 estimate in the context of 3D multi-echo acquisitions.

Methods: The impact of the spoiling regime was investigated through numerical simulations, phantom and *in vivo* experiments.

Results: The predicted dependence of T_1^{app} on tissue properties, system settings, and spoiling conditions was observed in both phantom and *in vivo* experiments. Diffusion effects modulated the dependence of T_1^{app} on both B_1^+ efficiency and T_2 times.

Conclusion: Error in T_1^{app} can be minimized by using an RF spoiling increment and gradient spoiler moment combination that minimizes T_2-dependence and safeguards image quality. Although the diffusion effect was comparatively small at 7T, correction factors accounting for this effect are recommended.

KEYWORDS

7T, EPG, imperfect spoiling, MPM, T1 mapping, VFA

1 | INTRODUCTION

Quantitative MRI (qMRI) is a powerful tool for investigating human brain microstructure *in vivo*. Key physical properties of the tissue can be quantified by combining weighted images with an appropriate physical model of the MRI signal.[1] This approach has been used to generate *in vivo* markers of myelin and iron distributions in the brain, see Edwards et al for a review,[2] and the sensitivity of the longitudinal relaxation time, T_1, to myelin content[3] has enabled the *in vivo* investigation of structure-function relationships.[4-7]

The variable flip angle (VFA) approach is a time-efficient method that combines a minimum of two spoiled gradient echo (SPGR) sequences, with different nominal flip

angles, to estimate T_1. Several variants, based on regression (DESPOT$_1$[8-11]), numerical minimization,[12] or using a closed form solution,[13,14] exist to combine these data. While the approach of Heule et al[12] provides an analytical solution for the steady-state SPGR signal that accounts for RF spoiling,[15] all others assume perfect spoiling, that is, that no transverse magnetisation persists across repetition times (TRs). In practice, gradient and radiofrequency (RF) spoiling are used to improve the validity of this assumption. Nonetheless, it is rarely met, leading to erroneous apparent T_1 estimates (T_1^{app}).

The most commonly used RF spoiling scheme relies on quadratically incrementing the RF pulse phase according to $\phi_n = \frac{\phi_0}{2}(n+1)n$ where n is the repetition number and ϕ_0 is the RF spoiling increment,[16] which has been shown to influence the error in T_1^{app}.[17] In gradient spoiling, voxels are assumed to consist of uniformly distributed isochromats, such that the MR signal sums to zero when the phase distribution imparted across the voxel is an integer multiple of 2π. This spoiling mechanism, and its impact on T_1^{app}, is amplified by diffusion effects as previously demonstrated in phantoms using large gradient moments.[18] However, achieving large moments is demanding on gradient performance and greatly extends the minimum achievable TR, running the risk of negating the benefit of these rapid imaging sequences.

Correction schemes have been proposed to recover the true T_1 from T_1^{app} at 3T.[17,19] These use Bloch simulations to model the impact of imperfect spoiling and derive correction factors that depend on the transmit field efficiency $f_{B_1^+}$. They assume an expected T_2 and the likely range of T_1 times and transmit field efficiencies, but to date have neglected diffusion effects.

It is unclear how imperfect spoiling will impact T_1 estimation at 7T, given T_2 shortens but T_1 and $f_{B_1^+}$ inhomogeneity increase. The sensitivity of 7T is often used to increase resolution. Imparting large spoiler moments across small voxel dimensions is increasingly demanding in terms of time and gradient performance. Considering these points, this study aimed to combine simulations and experiments to answer the following questions at 7T:

1. How do RF and gradient spoiling interact and which combination maximises the accuracy and precision of VFA-based T_1 mapping?
2. What impact does the diffusion effect have when considering clinically feasible gradient moments and the impact of the full readout?
3. What are the limitations of applying simulation-derived correction factors to recover the true T_1 from T_1^{app}?

We address these questions in the context of the multi-parameter mapping (MPM) protocol, which uses a 3D multi-echo VFA technique to quantify T_1^{app} and subsequently

correct for imperfect spoiling.[17,20,21] The multi-echo readout allows the flip angle-dependent signal intensity at echo time (TE) = 0 ms to be estimated together with T_2^*. The impact of different RF and gradient spoiling combinations on T_1^{app} are investigated as is the robustness of correcting for imperfect spoiling in post-processing when tissue and sequence parameters vary.

2 | METHODS

2.1 | Simulating the sensitivity of T_1^{app} to imperfect spoiling

The SPGR signal was simulated using the EPG formalism (https://sycomore.readthedocs.io/)[22] incorporating the diffusion-driven spoiling effect[23] imparted by the readout and spoiler gradients, applied on the same axis. A net dephasing of *nPi* was simulated per TR and varied from 2π to 10π with an increment of 2π. RF spoiling was simulated with increments ϕ_0 varying from 0° to 179° with an increment of 1°. A wide range of $f_{B_1^+}$, 40% to 160% with an increment of 30%, was simulated to capture increased transmit field inhomogeneity at 7T. Magnetization transfer (MT) effects were not included in the simulations.

Two SPGR signals, S_1 and S_2, were simulated with a TR of 19.50 ms and flip angles $\alpha_1 = 6°$ and $\alpha_2 = 26°$, respectively. T_1^{app} was estimated using the exact analytical expression[14]:

$$T_1^{app} = -\frac{TR}{\ln(E_1)} \text{ with}$$

$$E_1 = \frac{S_2 - \frac{S_1 \sin\alpha_2^c}{\sin\alpha_1^c}}{S_2 \cdot \cos\alpha_2^c - S_1 \cdot \frac{\cos\alpha_1^c \cdot \sin\alpha_2^c}{\sin\alpha_1^c}} \text{ and } \begin{cases} \alpha_1^c = \alpha_1 \cdot \frac{f_{B_1^+}}{100} \\ \alpha_2^c = \alpha_2 \cdot \frac{f_{B_1^+}}{100} \end{cases} \quad (1)$$

This protocol was simulated for the range of T_1 and T_2 times reported for gray matter (GM) and white matter (WM) at 7T: T_1 varying from 1000 ms to 2000 ms with a step of 250 ms[24-27] and T_2 varying from 35 to 55 ms with an increment of 5 ms.[28] The diffusion coefficient, D, was varied between 0.6 μm²/ms and 1 μm²/ms with an interval of 0.1 μm²/ms.[29,30] This protocol was also simulated for the phantom used in this study: $T_1 = 950$ ms, $T_2 = 60$ and 80 ms, D = 1.7 μm²/ms.

The error in T_1^{app} relative to the true T_1 was computed as: $\varepsilon(p) = 100 * \frac{T_1^{app}(p) - T_1^{true}}{T_1^{true}}$ with p a vector of simulation parameters, that is, $p = \left[T_1^{true}, T_2, D, nPi, \phi, f_{B_1^+}\right]$.

The SD of the error with all but one parameter fixed is used as a proxy to evaluate the sensitivity of T_1^{app} to that

parameter. For example, the sensitivity to T_2 was computed as follows:

$$Sensitivity_{T_2}\left(T_1^{true}, D, nPi, \phi, f_{B_1^+}\right) = \sqrt{\frac{1}{N_{T2}}\sum_{\text{All}T_2}\left(\varepsilon\left(p\right) - \overline{\varepsilon}\left(p\right)\right)^2}$$

(2)

Where $\overline{\varepsilon}\left(p\right) = \frac{1}{N_{T2}}\sum_{\text{All}T_2}\varepsilon\left(p\right)$ and N_{T2} the number of T_2 times simulated.

2.2 | Estimating correction parameters for imperfect spoiling

For a given set of parameters (T_2, D, ϕ_0 and nPi), correction factors were estimated as described in Ref. 17:

1. For every $f_{B_1^+}$, coefficients $A\left(f_{B_1^+}\right)$ and $B\left(f_{B_1^+}\right)$ were estimated by linear regression:

$$T_1 = A\left(f_{B_1^+}\right) + B\left(f_{B_1^+}\right) \cdot T_1^{app}$$

(3)

2. A second degree polynomial was fitted to the coefficients A and B:

$$\begin{cases} A = a_2 f_{B_1^+}^2 + a_1 f_{B_1^+} + a_0 \\ B = b_2 f_{B_1^+}^2 + b_1 f_{B_1^+} + b_0 \end{cases}$$

A set of coefficients $\left(a_i, b_i, i \in [0, 1, 2]\right)$ was computed for every pair $\left(\phi_0, nPi\right)$ based on simulations with different T_2 and D combinations applicable to both *in vivo* and phantom experiments (Table 1A).

2.3 | Image artifact due to imperfect spoiling

Gradient spoiling assumes uniformly distributed isochromats within a voxel, which is violated by partial voluming with different (or no) isochromats.[31] Bloch simulations, neglecting diffusion, were used to simulate a 1D grid of 100 isochromats with $T_1 = 1500$ ms and $T_2 = 45$ ms. Sequence parameters matching the *in vivo* acquisitions, described later, were adopted with $\phi_0 = 50°$ or $117°$. An off-resonance frequency of 1 kHz was attributed to one quarter of the spins, mimicking partial voluming of fat and water at 7T. The simulated signal was computed, for each TR, as the integral of the transverse magnetisation. The signal phase was plotted as a function of both phase-encoding directions, labeled partitions (inner loop, 120 acquired) and lines (outer loop, 192 acquired).

2.4 | Acquisitions

All data were acquired on a Siemens 7T Terra using a head coil with 8 transmit and 32 receive channels (Nova Medical).

2.4.1 | Reference measurements

Reference T_1 and T_2 maps were obtained from single-slice spin-echo echo-planar-imaging (EPI) acquisitions with (IR-SE-EPI) and without (SE-EPI) inversion preparation, respectively. Key parameters were: TR = 10 s, in-plane field of view (FOV) of 192×192 mm^2 with 1.2×1.2 mm^2 in-plane resolution, slice thickness of 3.5 mm, acceleration factor of 3 and partial Fourier (6/8). To estimate T_2, 13 acquisitions were obtained with variable TE (29, 34, 39, 44, 49, 59, 69, 79, 89, 99, 109, 119, or 129 ms). To estimate T_1, data were acquired with 10 inversion times (100, 170, 200, 280, 470, 780, 1300, 2100, 3600, or 5000 ms) with a fixed TE of 29 ms.

The apparent diffusion coefficient (ADC) was measured with diffusion-weighted spin-echo EPI acquisitions. Key parameters were: 34 axial slices, 1.4 mm isotropic resolution, TE/TR = 63/3700 ms, multiband factor 2, in-plane acceleration factor 2, fat saturation preparation. Three acquisitions with diffusion encoding along x, y or z, were obtained with b-values of 1000 s/mm^2, 700 s/mm^2 or 0 s/mm^2. T_2 and ADC were estimated with a mono-exponential decay using a log-linear fit and T_1 was estimated with a nonlinear least-squares fit to the inversion recovery signal equation.

2.4.2 | MPM protocols

The SPGR data were acquired with an in-house sequence at 1 mm isotropic resolution over a FOV of $192 \times 192 \times 160$ mm^3 using settings that matched the simulations. Flip angles of $\alpha_1 = 6°$ (referred to as "PDw") and $\alpha_2 = 26°$ ("T_1w") were achieved with rectangular excitation pulses of duration 80 μs and 1500 μs, respectively, to match the pulse power $B_1^2 \times$ pulse duration. Six echoes were acquired with TE ranging from 2.56 ms to 11.66 ms in steps of 1.82 ms using a TR of 19.5 ms. The spoiler gradient moment was varied across protocols by changing its duration. Elliptical sampling and partial Fourier (6/8) in both phase-encoding directions were used to achieve tolerable session durations. Elliptical sampling was only turned off for Session 6 (c.f. Table 1B).

$f_{B_1^+}$ was mapped using an in-house sequence exploiting the Bloch-Siegert shift[32] and reconstructed in real-time with in-house code implemented in Gadgetron.[33] Relevant parameters were: single echo, TE/TR = 6.77/40 ms, 14° flip angle,

TABLE 1 A, Parameters used to determine the correction factors for phantom and *in vivo* acquisitions. B, Data acquired in each of the 7T imaging sessions

A. Correction factors

Set	$f_{B_1^+}$ [%]	In vivo				Phantom		
		T_1 [ms]	T_2 [ms]	D [μm^2/ms]	T_1 [ms]	T_2 [ms]	D [μm^2/ms]	
1	40:30:160	1000:150:2000	35	0.8	650:150:1250	60	1.7	
2	40:30:160	1000:150:2000	45	0.8	650:150:1250	80	1.7	
3	40:30:160	1000:150:2000	55	0.8	650:150:1250	60	0	
4	40:30:160	1000:150:2000	35	0				
5	40:30:160	1000:150:2000	55	0	*(min:step:max)*			

B. Acquisitions

In vivo	Sequence	FA [°]	Φ_0 [°]	nPi [π]	Voltage	Sampling	Acquisition time [min]	Phantom
Session 1,2,3,4	SPGR	6	50,117,120, 144	2	×1	elliptical	5.01	✓
	SPGR	26	50,117,120, 144	2	×1	elliptical	5.01	✓
	SPGR	6	50,117,120, 144	6	×1	elliptical	5.01	✓
	SPGR	26	50,117,120, 144	6	×1	elliptical	5.01	✓
	BSS				×1	elliptical	3.52	✓
	SPGR	6	50,117,120, 144	2	×1.6	elliptical	5.01	✗
	SPGR	26	50,117,120, 144	2	×1.6	elliptical	5.01	✗
	SPGR	6	50,117,120, 144	6	×1.6	elliptical	5.01	✗
	SPGR	26	50,117,120, 144	6	×1.6	elliptical	5.01	✗
	BSS		50,117,120, 144		×1.6	elliptical	3.52	✗
Session 5	SPGR	26	117	6	×1	elliptical	5.01	✗
Session 6	SPGR	26	50	2	×1	full	5.42	✗
	SPGR	26	50	6	×1	full	5.42	✗
	SPGR	26	117	2	×1	full	5.42	✗
	SPGR	26	117	6	×1	full	5.42	✗
Session 7	SE-EPI	1 slice, 13 TEs, variable B_1^+ region					13	✓
	SE-EPI	1 slice, 13 TEs, homogeneous B_1^+ region					13	✗
	IR-SE-EPI	1 slice, 10 TIs, variable B_1^+ region					10	✓
	IR-SE-EPI	1 slice, 10 TIs, homogeneous B_1^+ region					10	✗
	DW-SE-EPI	32 slices , 3 b-values					0.5	✓

BSS = Bloch-Siegert Shift based B_1^+ mapping.

FOV of $256 \times 256 \times 192$ mm^3 with 4 mm isotropic resolution. The B_1^+-encoding was achieved with a Fermi pulse of duration 2 ms, 2 kHz off-resonance frequency and 190° flip angle. An RF spoiling increment of 90° was used as required for the interleaved acquisition scheme with short TR adopted here.[34]

2.4.3 | Imaging sessions

To evaluate the effects in a simplified scenario, a phantom was constructed of 1.5% (w/v) agarose in a 1 mM copper sulphate solution. Reference T_1, T_2, and ADC measurements were acquired, along with T_1 mapping data using the eight MPM protocols ($4\Phi_0 \times 2$ *nPi*).

To evaluate the effects *in vivo*, reference and MPM data were acquired in a healthy volunteer (female, 40 y), with approval from the local ethics committee. Each MPM protocol was repeated with the transmitter's reference voltage increased by 60% to test the simulation-based hypothesis that the impact of the T_2 used in the imperfect spoiling correction would increase at higher $f_{B_1^+}$. Additional scanning sessions were performed to facilitate co-registration to an independent data set and to explore the impact of k-space sampling on image artifacts. The acquisitions are summarised in Table 1B.

2.4.4 | T_1 estimation

A modified version of the hMRI toolbox (hMRI.info)[20] was used to process each PDw/T_1w pair acquired under the same conditions, that is, consistent nPi, ϕ_0 and reference voltage. The PDw and T_1w signals at TE = 0 were estimated from the log-linear fit of the echoes from both contrasts[35] and used to estimate T_1^{app}, using Equation (1) and correcting for $f_{B_1^+}$ with the corresponding B_1^+ map. A total of 8 T_1^{app} maps were computed for the phantom (2 nPi × 4ϕ_0) and 16 for the *in vivo* case (2 nPi × 2 transmitter voltages × 4ϕ_0).

Corrected phantom T_1 maps were constructed for each of the eight acquisition conditions by applying three sets (two T_2 values with diffusion, and one without) of simulation-based imperfect spoiling correction parameters calculated for the corresponding combination of ϕ_0 and nPi resulting in 24 corrected T_1 maps. Corrected *in vivo* T_1 maps were also constructed for each condition by applying five sets of correction factors (three T_2 values with diffusion, and two without) resulting in 80 corrected T_1 maps.

2.5 | Analysis

In vivo, one acquisition per session (T_1w, echo 1, $nPi = 6\pi$, nominal voltage) was segmented using SPM12.4.[36] GM and WM masks were defined by those voxels for which the probability of belonging to the given tissue class exceeded 0.9. Global GM and WM masks were computed from the intersection of these session-specific masks.

To ensure equivalent processing, particularly spatial interpolation, each T_1 and B_1^+ map was co-registered to the T_1-weighted image acquired independently in Session 5. Separately, the 3D T_1 maps were co-registered to the single-slice reference maps with SPM12.6, which supports 2D input as reference for 3D volumes.

2.5.1 | Phantom

To investigate the dependence of T_1^{app} on $f_{B_1^+}$, voxels were partitioned into 5% $f_{B_1^+}$ intervals. The median T_1^{app} was computed per bin, plotted against $f_{B_1^+}$ and compared to simulations using $T_2 = 80$ ms, D = 1.7 μm^2/ms and $T_1 = 950$ ms. The same analysis was performed on the corrected T_1 maps.

2.5.2 | In vivo

The dependence of T_1^{app} on $f_{B_1^+}$ was investigated for each MPM protocol, with the nominal transmitter reference voltage. To minimize confounding anatomical variability, the analysis was restricted to voxels for which the reference T_1 time was between 1100 ms and 1350 ms in the slice with greatest transmit field inhomogeneity (Supporting Information Figure S1, which is available online). Voxels were partitioned into 2% $f_{B_1^+}$ intervals. The results were compared to simulations using the mean reference values (ie, $T_2 = 45$ ms, D = 0.8 μm^2/ms and $T_1 = 1250$ ms).

To investigate the dependence of T_1^{app} on T_2, the reference T_2 map was used to partition voxels into 2 ms intervals across the T_2 range. To minimize uncontrolled $f_{B_1^+}$ variance, the reference slice with least transmit field inhomogeneity was used (Supporting Information Figure S1). $f_{B_1^+}$ dependence was investigated by analysing both the nominal and high (x1.6) transmitter voltage T_1^{app} maps. The analysis was again restricted to voxels with reference T_1 between 1100 and 1350 ms to minimize anatomical variability. Median T_1^{app} per bin was computed for each imaging scenario (nPi, ϕ_0 and transmitter voltage), plotted against T_2 and compared to simulations with D = 0.8 μm^2/ms, $T_1 = 1250$ ms and $f_{B_1^+} = 70$ and 130%.

For each *in vivo* T_1 map, from each of the MPM sessions, the distribution of T_1^{app} and corrected T_1 times within GM and WM were plotted for voxels with $f_{B_1^+}$ between 95% and 105% according to the nominal voltage $f_{B_1^+}$ map.

3 | RESULTS

3.1 | Simulated error in T_1^{app}: dependence on B_1^+ efficiency and tissue properties

With parameters in the middle of their simulated ranges (Figure 1A), T_1^{app} matched the true T_1 when ϕ_0 was approximately 15°, 89°, 91°, 117°, 123°, and 174° when $nPi = 2\pi$. Slightly different ϕ_0 were required if nPi differed. Overestimation of T_1 peaked at 6% with $\phi_0 = 30°$ and $nPi = 2\pi$.

Higher $f_{B_1^+}$ and D, coupled with shorter T_2 and T_1, required markedly different ϕ_0 (26°, 118°, 123°, and 171°) for T_1^{app} to match the true T_1 (Figure 1B), although dependence on nPi was reduced. However, the error was larger with overestimation peaking at 10% with $\phi_0 = 48°$.

Overall, no ϕ_0 and nPi combination provided accurate T_1 estimates for all tissue properties and B_1^+ efficiencies. The impact of gradient spoiling on the error was variable across the different conditions simulated.

T_1^{app} was most sensitive to $f_{B_1^+}$ (Figure 1C). The degree of sensitivity was highly dependent on ϕ_0. It reached 6% for the commonly used value of 50°, but fell below 2% for 117° when T_2, T_1, and D were fixed to 45 ms, 1500 ms, and 0.8 μm^2/ms, respectively.

Sensitivity to T_2 (and T_1) was markedly lower falling below 2% (and 1%) for most ϕ_0 when $f_{B_1^+}$ was optimal (ie, 100%, Figure 1D,F) but increased to 4% (and 3%) when $f_{B_1^+}$ was 160% (Figure 1E,G).
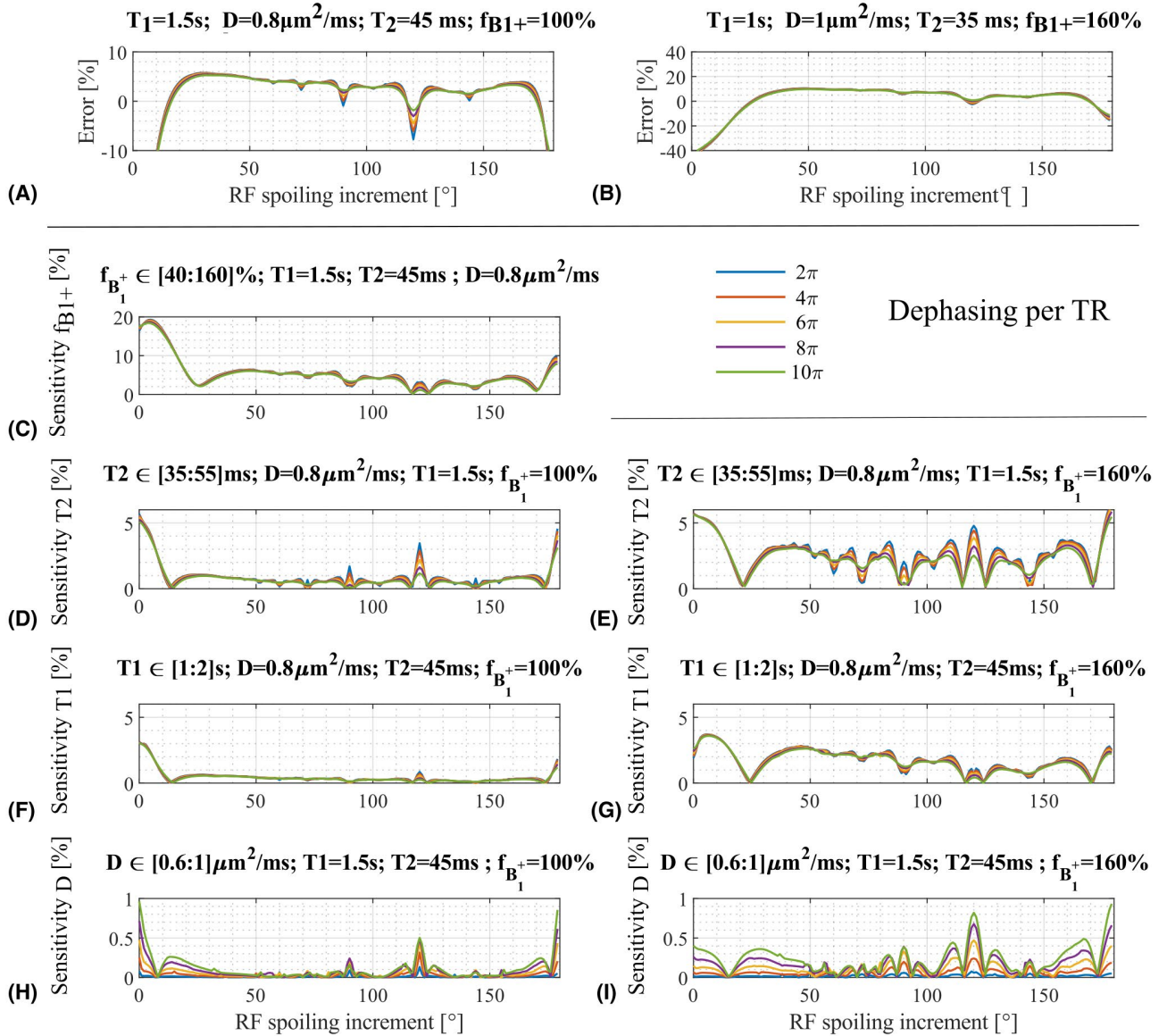
FIGURE 1 Numerical simulations, for each spoiling condition, of T_1^{app} error (ε) in two specific cases: $T_1 = 1.5$ s, D = 0.8 μm^2/ms, $T_2 = 45$ ms, and $f_{B_1^+} = 100\%$ (A); $T_1 = 1$ s, D = 1 μm^2/ms, $T_2 = 35$ ms, and $f_{B_1^+} = 160\%$ (B). Sensitivity of T_1^{app} to B_1^+ efficiency (C), the true T_2 time (D-E), the true T_1 time (F-G), and the diffusion coefficient (H-I). The sensitivity to T_1, T_2, and D are computed in two conditions: B_1^+ efficiency of 100% (D-F-H) or 160% (E-G-I)

T_1^{app} was least sensitive to D over the range of values tested. With T_1 and T_2 of 1500 ms and 45 ms, respectively, the maximum sensitivity did not exceed 1%, even for high $f_{B_1^+}$ (Figure 1H,I). Higher nPi increased sensitivity to D.

For some ϕ_0, the sensitivity to T_2, T_1 and $f_{B_1^+}$ decreased as nPi increased (eg, 110° and 85°), whereas for others the opposite was true (eg, 60° and 72°).

## 3.2 | Simulated error in T_1: impact of correction parameters

Correction factors derived from numerical simulations with $T_2 = 45$ ms and D = 0.8 μm^2/ms dramatically decreased the

error in T_1^{app} (c.f. Figures 1A and 2 middle row). However, the amplitude of the residual error was amplified by high $f_{B_1^+}$ and depended on whether the T_2 used to derive the correction factors (45 ms) matched that of the simulation (Figure 2). For the commonly used ϕ_0 of 50°, a discrepancy in T_2 of 10 ms coupled with $f_{B_1^+} = 160\%$ had a residual error of 2.7%.

Some RF spoiling increments were more robust to the choice of T_2 and had lower residual error that further decreased by increasing the spoiler gradient moment. For the optimal combination of $\phi_0 = 144°$ and $nPi = 6\pi$ the correction parameters reduced the error to less than 0.8% for the full range of parameters investigated (Figure 2).

The particularly low T_2 sensitivity of 144° motivated its use in subsequent experiments. 120° was additionally

FIGURE 2 Residual errors after applying imperfect spoiling correction parameters derived with $T_2 = 45$ ms and $D = 0.8$ μm^2/ms to T_1^{app}. T_1^{app} was estimated from data simulated with a true T_1 time of 1.5 s, and a true T_2 time ranging from 35 to 55 ms for $nPi = 2\pi$ (dashed lines) or 6π (solid lines). Each row corresponds to a different B_1^+ efficiency, $f_{B_1^+}$, ranging from 40 to 160%. The error is minimized when the T_2 used to estimate the correction parameters matches the true T_2 (ie, 45 ms). Dashed vertical lines indicate the RF spoiling increments used in the in vivo acquisitions (ie, 50°, 117°, 120°,and 144°)
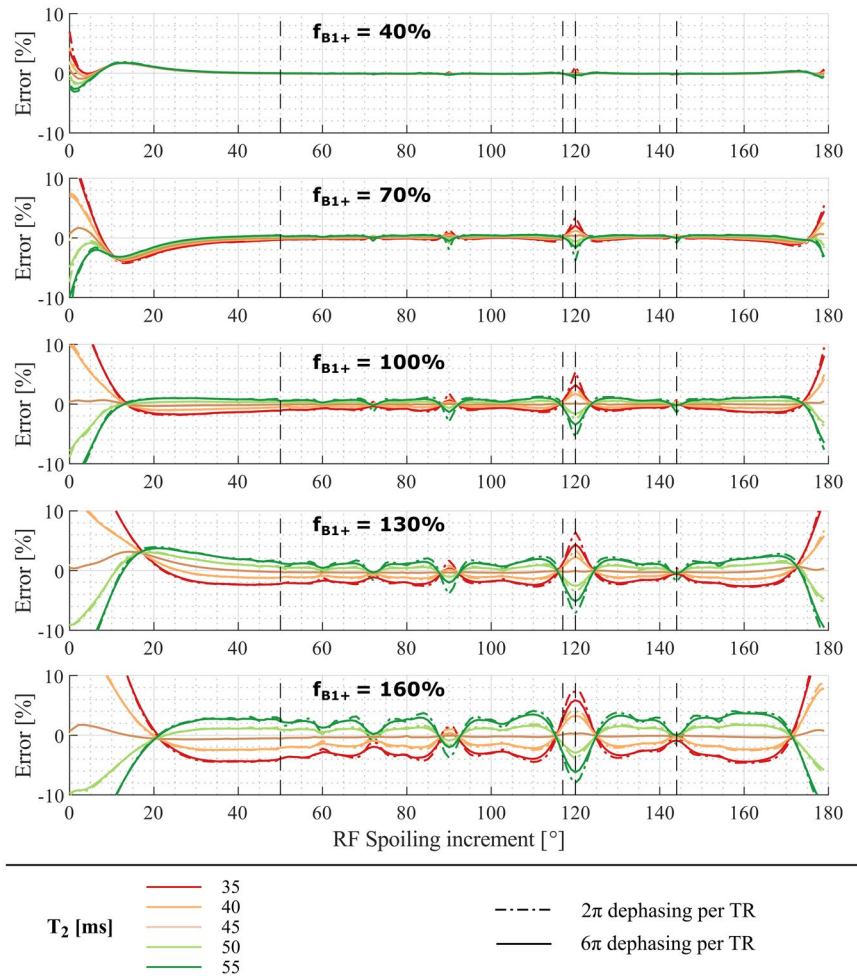
3.3 | Comparison between simulation and phantom experiment

Reference T_2, T_1 and ADC values in the phantom were estimated to be 78 ± 2 ms, 952 ± 14 ms and 1.71 ± 0.04 μm^2/ms, respectively.

The $f_{B_1^+}$ dependence of T_1^{app} (Figure 3A,B,F,G) matched the numerical simulations. T_1^{app} increased with $f_{B_1^+}$ for 50° (+50 ms) but decreased for 120° (−96 ms), and 117° (−77 ms), while 144° showed least sensitivity (−30 ms). The $f_{B_1^+}$ dependence of the increments of 120° and 144° was impacted by the increase of the spoiler gradient moment, whereas it had no observable impact for 117° and 50°.

T_1^{app} maps were corrected with three sets of correction factors. The maps corrected with a T_2 of 80 ms showed almost no $f_{B_1^+}$ dependence but had a ϕ_0-dependent offset (Figure 3C,H), which was removed when T_2 was reduced to 60 ms (Figure 3D,I). However, when the correction factors were

computed without accounting for diffusion, the corrected T_1 again showed ϕ_0-dependent offsets, particularly with a large spoiler gradient moment (Figure 3E,J).

3.4 | Comparison between simulation and in vivo experiment

Reference T_2, T_1 and ADC value in the WM region used for subsequent analyses were estimated to be 47 ± 6 ms, 1260 ± 50 ms and 0.7 ± 0.1 μm^2/ms, respectively.

The dependence of T_1^{app} on $f_{B_1^+}$ (Figure 4A,C) predicted by simulation was observed *in vivo* (Figure 4B,D). ϕ_0 of 50° and 120° were most sensitive to $f_{B_1^+}$ with T_1^{app} varying by +41 ms or −40 ms, respectively, between 65 and 110% efficiency. The variation was 24 ms for 117° and 5 ms for 144°. As predicted, increasing the gradient spoiler moment had the biggest impact on 120°, for which the T_1^{app} variation decreased to −15 ms over the range of $f_{B_1^+}$.

Simulations predicted that, as T_2 increased, T_1^{app} would be under-estimated for $\phi_0 = 120$° or slightly over-estimated for $\phi_0 = 50$° (Figure 5). A small T_2-dependence was predicted for 117° and even less so for 144°. These dependencies were
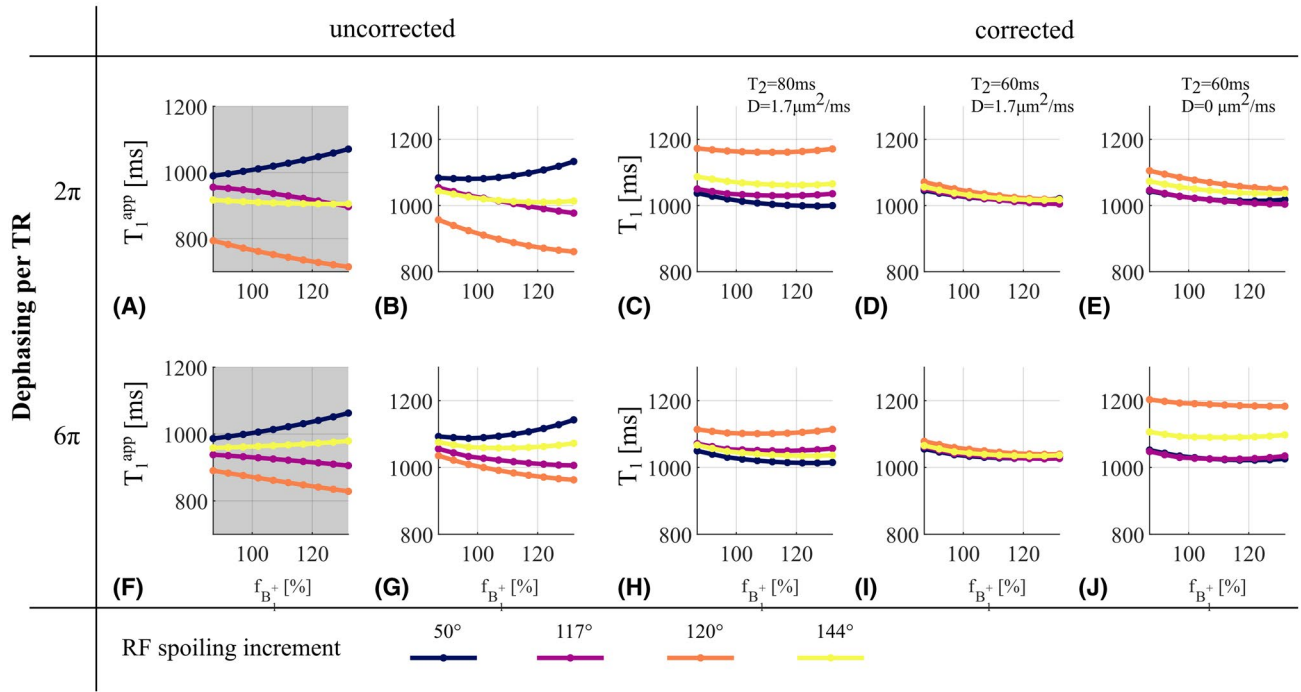
FIGURE 3 T_1^{app} (A,B,F,G) and corrected T_1 (C,D,E,H,I,J) in the phantom with $\phi_0 \in [50, 117, 120, 144]°$, as a function of the B_1^+ efficiency, $f_{B_1^+}$. Dephasing across a voxel of 2π (A-E) and 6π (F-J) per TR are shown. A,F, Numerical simulations. Fixed parameters are: $T_1 = 950$ ms, $T_2 = 80$ ms, $D = 1.7$ μm^2/ms. B-E,G-J, Acquisitions. Corrected T_1 with correction factors from set 1 (C,H), set 2 (D,I), and set 3 (E,J) from Table 1A
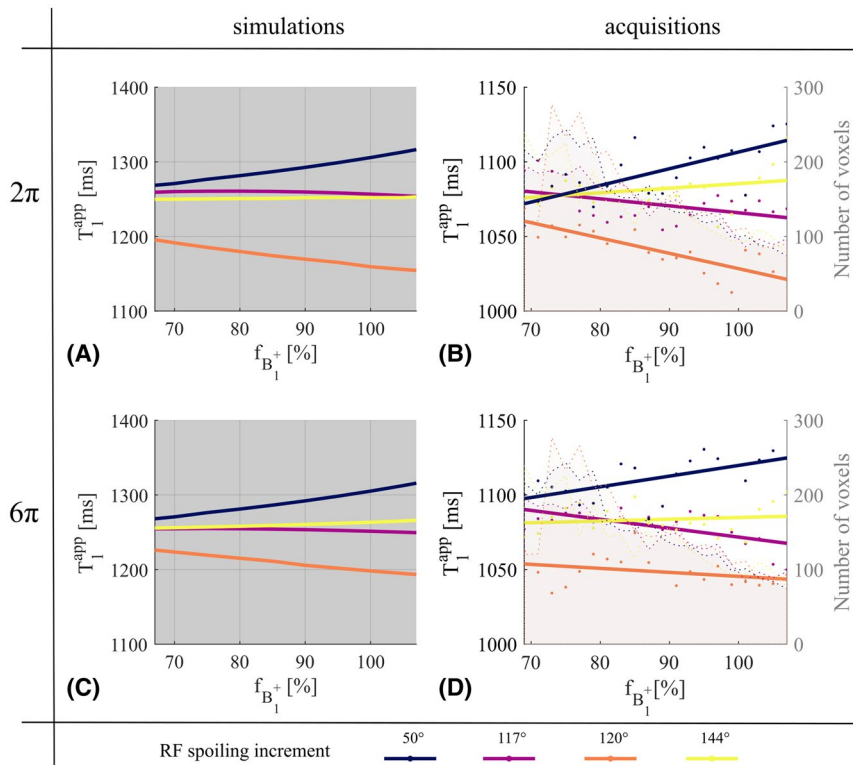
FIGURE 4 *In vivo* T_1^{app}, obtained with $\phi_0 \in [50, 117, 120, 144]°$, as a function of the B_1^+ efficiency, $f_{B_1^+}$. Dephasing across a voxel of 2π (A,B) and 6π (C,D) per TR are shown. A,C, Numerical simulations. Fixed parameters are: $T_1 = 1250$ ms, $T_2 = 45$ ms, $D = 0.8$ μm^2/ms. B,D, Acquisitions, and linear fitting for illustration purposes. The number of voxels included in each bin is depicted by the shaded background of each graph for each ϕ_0

predicted to be accentuated when $f_{B_1^+}$ increased to 130% and to be reduced when nPi was increased from 2π to 6π. Most of those predictions were observed *in vivo*: over the T_2 range, with 2π gradient spoiling, T_1^{app} decreased by 51 ms for 120°

and increased by 30 ms for 50°. This reduced to 12 and 25 ms, respectively, for 6π. The variation of T_1^{app} for 117° and 144° did not exceed 20 ms. Discrepancies between simulations and acquisitions occurred in the case of high $f_{B_1^+}$ and
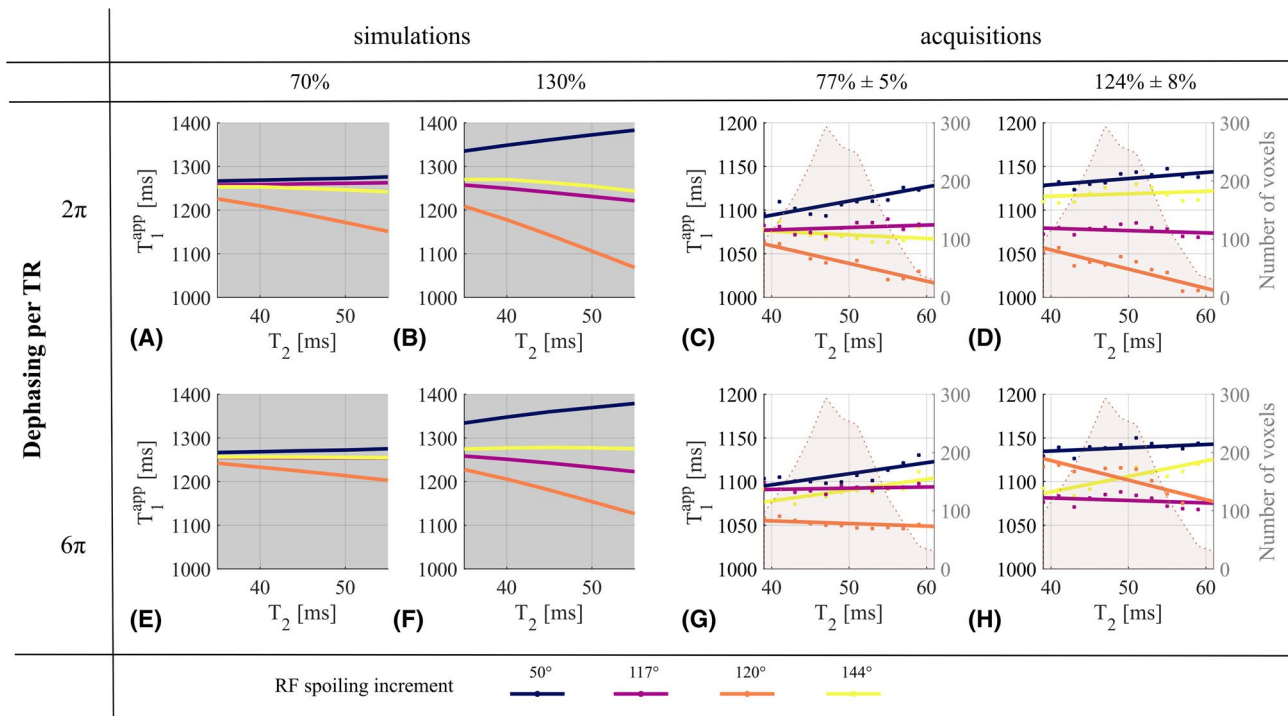
FIGURE 5 *In vivo* T_1^{app}, obtained with $\phi_0 \in [50, 117, 120, 144]°$, as a function of T_2. Dephasing across a voxel of 2π (A-D) and 6π (E-H) per TR are shown. Original ($\times 1$) (A,C,E,G) and high ($\times 1.6$) (B,D,F,H) transmitter reference voltage are shown. A,B,E,F, Numerical simulations. Fixed parameters are: $T_1 = 1250$ ms, $D = 0.8$ μm^2/ms, $f_{B_1^+} = 70\%$, and 130% as measured in the transmit field map in the slice of interest. C,D,G,H, Acquisitions, and linear fitting for illustration purposes. The number of voxels included in each bin is depicted by the shaded background of each graph for each ϕ_0

gradient spoiling (Figure 5H). T_1^{app} showed the predicted reduction with increasing T_2 for 120°, but an unpredicted offset. An unpredicted increase was also observed for 144° while the increased T_2-dependence predicted for 50° was not observed (Figure 5D,H).

3.5 | Impact of correction parameters in vivo

Although the T_1 maps with different spoiling conditions, with and without correction for imperfect spoiling, were qualitatively similar (Figure 6), some distinct contrast differences were observed, for example, between GM and cerebrospinal fluid (green box) and within the basal ganglia (black box). The within-increment SD (σ_{row}) across T_1 maps revealed particularly high sensitivity to spoiling condition and the T_2 used to derive the correction parameters (c.f. Figure 6B ϕ_0 of 50° or 120° versus 117° or 144°). The T_1 maps converged (low σ_{col}, Figure 6C) when sufficient gradient spoiling ($nPi = 6\pi$) was combined with a T_2 of 35 ms to derive the correction parameters, but diverged (high σ_{col}, Figure 6C) when low spoiling ($nPi = 2\pi$) was combined with no correction for imperfect spoiling or one based on a T_2 of 55 ms.

The impact of correcting for imperfect spoiling increased with $f_{B_1^+}$ (Figure 7). The correction induced the largest shifts

in T_1 for ϕ_0 of 50° (Figure 7), especially when $f_{B_1^+} = 160\%$. The higher variance observed across conditions for this increment (Figure 6B) also exhibits a pattern consistent with the $f_{B_1^+}$ profile. $\phi_0 = 117°$ only benefited from correction at high $f_{B_1^+}$.

Corrected T_1 times were highly dependent on the T_2 used for the correction, especially when $f_{B_1^+}$ was 160%. A global T_2 time of 35 ms minimized dependence on ϕ_0 (Figure 6C). $\phi_0 = 120°$ was additionally dependent on D regardless of experimental conditions. $\phi_0 = 144°$ was exceptional in that the corrected T_1 times were effectively independent of the tissue properties (T_2 and D) used to determine the correction parameters.

3.6 | Artifact dependence on spoiling conditions

The weighted images used to calculate T_1 were affected by background artifacts when $nPi = 2\pi$ (Figure 8A). With rectangular k-space sampling, the artifact manifested as a coherent alias of brain edges. Its location depended on ϕ_0: the replica was shifted in the partition direction for 117°, but in both the partition and line directions for 50°. While still visible, the artifact was more diffuse with elliptical sampling (Figure 8A). Numerical simulations with rectangular
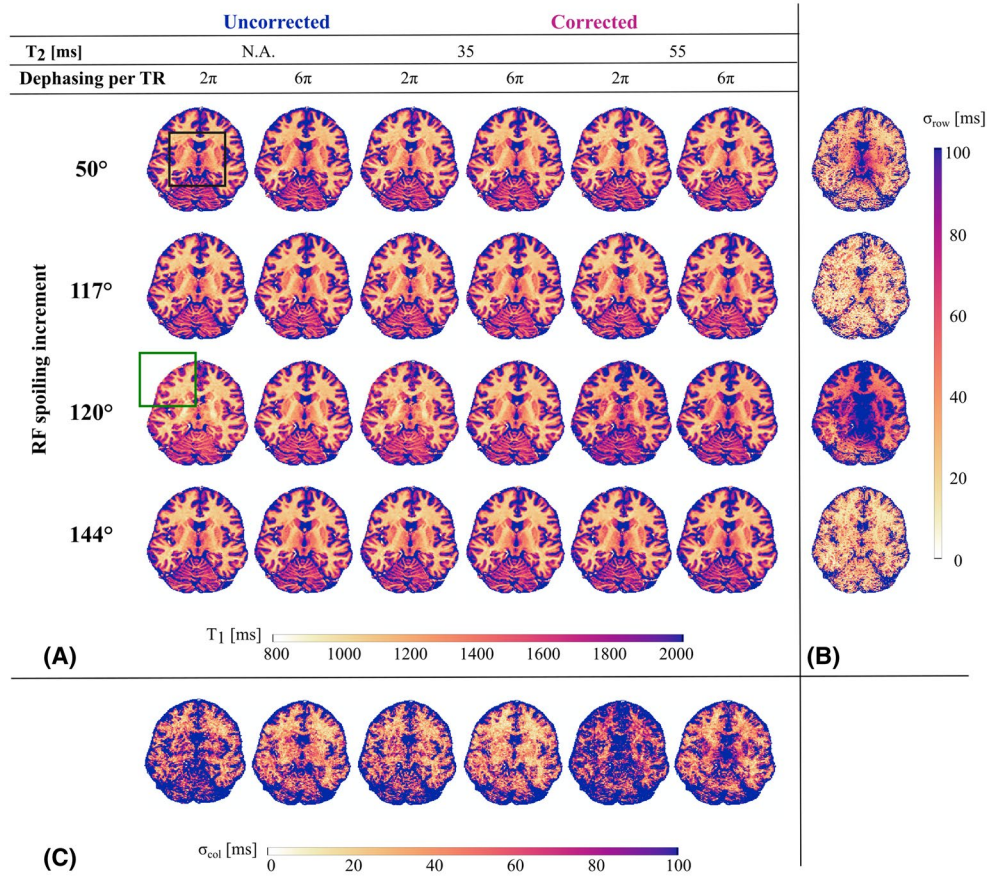
FIGURE 6 A, Axial view from T_1 maps obtained with nominal $f_{B_1^+}$ (ie, no reference voltage manipulation) and $nPi = 2\pi$ (columns 1, 3, and 5) or 6π (columns 2, 4, and 6) for each RF spoiling increment (rows). These are presented before (ie, T_1^{app}, columns 1 and 2) and after correction for imperfect spoiling using a fixed D of 0.8 μm^2/ms and a T_2 of either 35 ms (columns 3 and 4) or 55 ms (columns 5 and 6). Black and green boxes highlight areas particularly affected by changing nPi or applying correction factors. B, Maps of σ_{row}, the voxel-wise SD of T_1 across conditions for a given RF spoiling increment (ie, along rows in (A)). C, Maps of σ_{col}, the voxel-wise SD of T_1 across RF spoiling increments for a given condition (ie, along columns in (A))

k-space sampling based on a mixed population of isochromats (different resonance frequencies) showed phase variation across TR (Figure 8C). $\phi_0 = 117°$ produced a periodic phase variation across partitions consistent with the observed position of the ghost artifact in the field-of-view along this direction. $\phi_0 = 50°$ resulted in phase variation in both the lines and partitions directions, again consistent with the empirical data.

4 | DISCUSSION

We have demonstrated a complex relationship between the estimated T_1 and the spoiling regime within the context of the 3D VFA approach. Our simulations (Figure 1) indicate that no RF spoiling increment would lead to T_1^{app} matching the true T_1 across all conditions (ie, sequence choices, T_2 times, and diffusion coefficients). Furthermore, the simulations show that even the fullest effects of diffusion achieved

in a multi-echo acquisition are insufficient to achieve perfect spoiling of the transverse magnetisation.

The sensitivity to imperfect spoiling effects will depend on the specifics of the protocol used. It has recently been suggested that the maximum flip angle should be minimized to mitigate spoiling-induced errors.[37] However, for the TR and target T_1 range considered here, this would compromise the precision of the T_1 estimates by as much as 50%.[38] An alternative would be to reduce both flip angles and TR, which could be achieved by adopting a single echo protocol. However, simulations suggest that the sensitivity of such an approach would be on a par with that observed in the protocol used here (c.f. Figure 1 and Supporting Information Figure S2). Combining a single echo approach with a long TR and using the time to impart extensive gradient spoiling is predicted to reduce the sensitivity of T_1 estimates to imperfect spoiling, even in the case of high flip angles (Supporting Information Figure S2). However, unlike the multi-echo MPM protocol adopted here, single echo protocols prevent
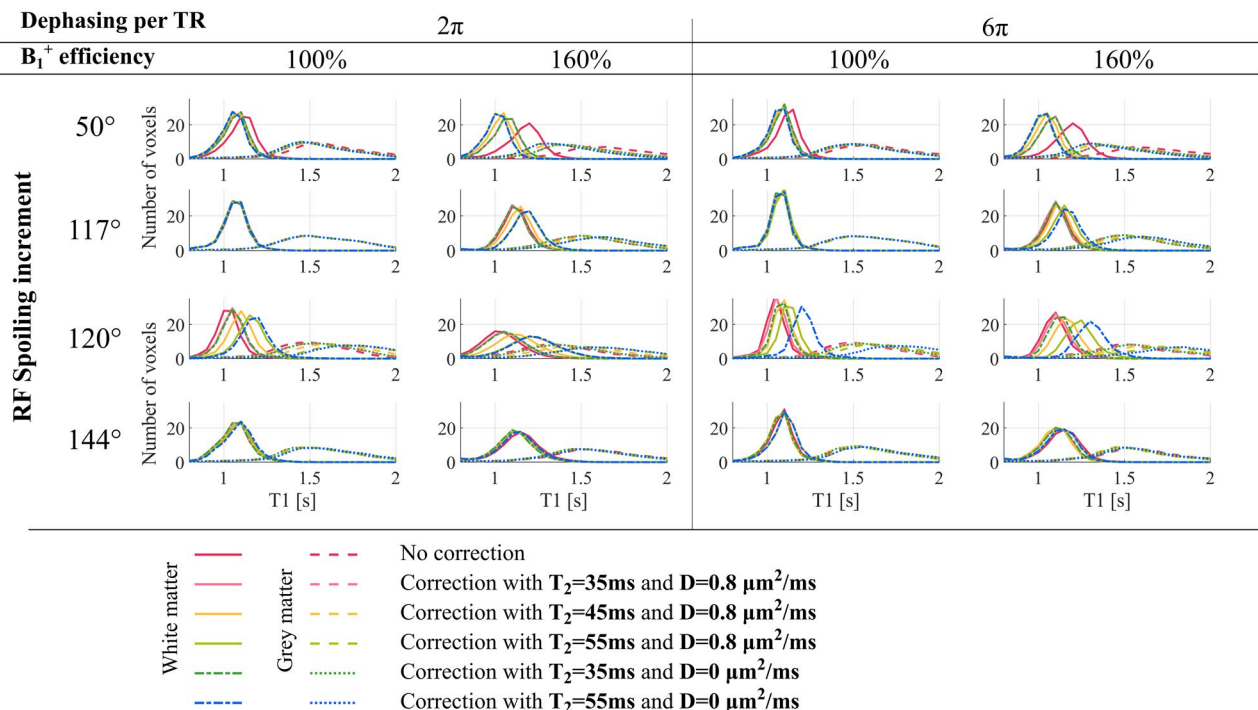
FIGURE 7 Histograms of the estimated T_1 times for WM and GM without (ie, T_1^{app}) and with correction for imperfect spoiling. Five sets of correction factors were computed based on different T_2 times and diffusion coefficients and applied separately. Only those voxels with $f_{B_1^+}$ between 95% and 105% (measured with no reference voltage manipulation) were included in the analysis

T_2^* from being concurrently estimated, and prevent extrapolation to TE = 0 ms, which aims to remove bias introduced by flip angle-dependent T_2^* decay[35,39] from the T_1 estimates. Slice-selective 2D acquisitions would naturally achieve a long TR and improved spoiling behaviour, but suffer limitations such as MT effects and imperfect slice profiles that lead to flip angle-dependent[40] bias in the T_1 estimates.

In the context of the MPM protocol investigated here T_1^{app} was most sensitive to $f_{B_1^+}$, which could lead to over-estimation of the true T_1 by as much as 30%. Despite accounting for $f_{B_1^+}$ inhomogeneity in both simulations and acquisitions (Equation 1), T_1^{app} continued to depend on $f_{B_1^+}$ in an increment-specific manner. Some ϕ_0, such as the commonly used 50°, were particularly sensitive (Figures 1,3 and 4), although the error can be markedly reduced by post-hoc correction for imperfect spoiling (Figures 2,3 and 6). Since the correction factors are a function of both T_1^{app} and $f_{B_1^+}$ (Equation 3), they rely on accurate estimation of the true $f_{B_1^+}$. Any error will propagate through to the corrected T_1 time. It may then be appealing to select a ϕ_0 that exhibits lower sensitivity to $f_{B_1^+}$, for example, 117° or 144° (Figures 1 and 3). However, the sensitivity of T_1^{app} to inaccurate or imprecise definition of the flip angles ($f_{B_1^+}$ in Equation 1) would remain.[41]

Other sources of $f_{B_1^+}$ dependence may affect the accuracy of the T_1 estimate, and were reduced as much as possible in this work:

1. MT effects, proportional to the square of the amplitude of the transmit field, have been shown to bias T_1^{app} [37,42,43] and can be expected to be a more significant problem at 7T. Experimentally, the MT effect was limited by the use of rectangular pulses with matched power for the PD- and T_1-weighted acquisitions. Nonetheless, residual dependence may remain and may underlie the offset between the T_1 measured in WM with the IR-SE-EPI (1260 ms) and VFA (~1100 ms) approaches. MT effects were not included in any of our simulations of the steady-state signal since it depends on a number of unknown, spatially varying tissue properties. However, we can estimate the impact of MT effects in the present context for WM using the EPG-X framework (https://github.com/mriphysics/EPG-X).[44,45] Assuming a bound pool fraction (BPF) of 0.117,[44] thermal equilibrium with an exchange rate from free to bound pool of 4.3 s^{-1},[44] and a T_1 time of 1.25 s for each pool, the MT effect caused T_1^{app} to decrease as $f_{B_1^+}$ increased. Depending on the RF spoiling increment used, this bias could either counteract (eg, $\phi_0 = 50°$) or accentuate (eg, $\phi_0 = 120°$) the $f_{B_1^+}$ sensitivity induced by imperfect spoiling (Figure 9B). However, the MT effect was largely independent of the RF spoiling increment (Figure 9A). A method has recently been proposed to counteract MT effects at the time of acquisition.[43]
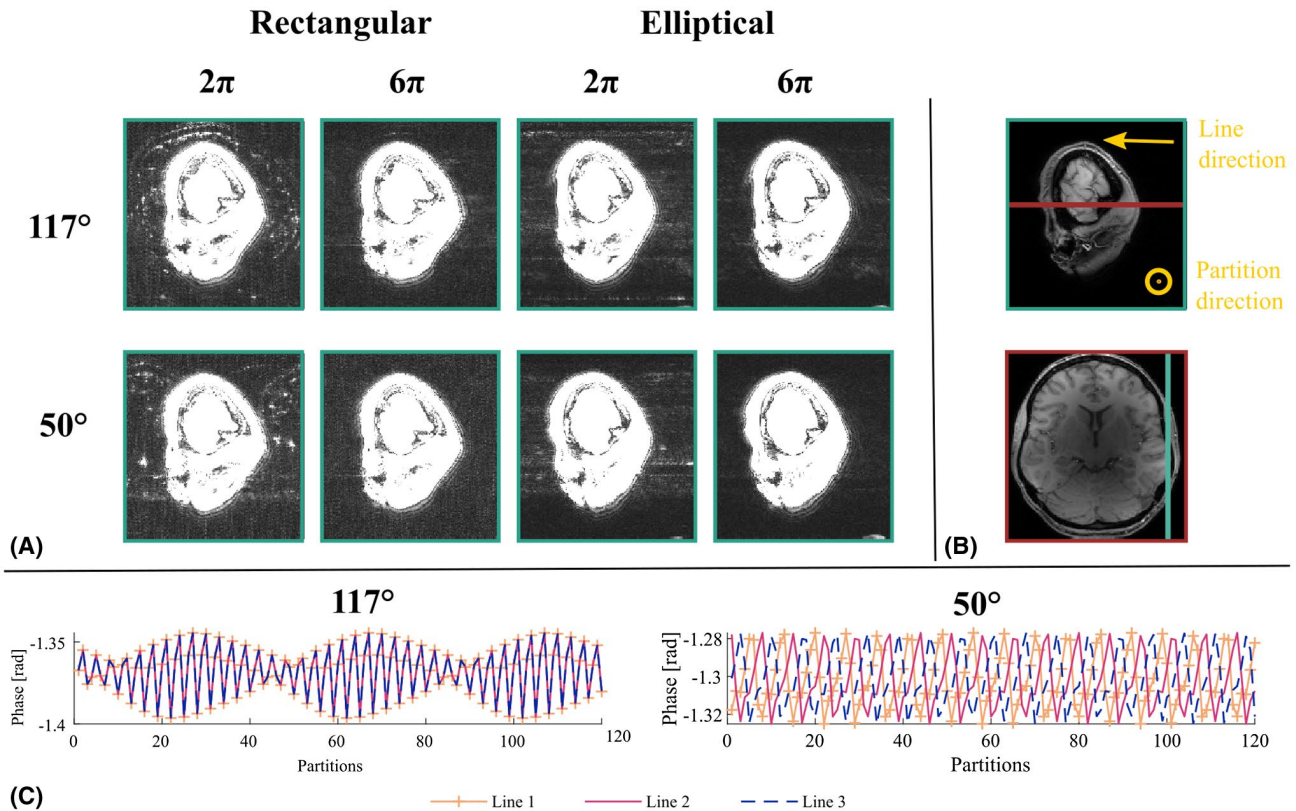
FIGURE 8 A, Sagittal view of T_1-weighted images acquired with rectangular or elliptical k-space sampling using different spoiling conditions. The images have been windowed to highlight background signal. B, The same sagittal slice and an axial slice are shown windowed to visualize the brain. The turquoise line in the axial view indicates the sagittal position while the red line on the sagittal view indicates the axial position. The two phase-encoding directions (lines and partitions) are indicated in the sagittal view. C, Numerical simulations of the impact of partial voluming on the phase of the signal across lines and partitions (rectangular sampling case, all partitions are acquired before incrementing the line) for each RF spoiling increment

2. T_2^* has previously been shown to depend on the excitation flip angle.[35] If differential T_2^* weighting exists in the SPGR signals Equation (1) will lead to biased T_1 estimates. Unlike single echo approaches, the multi-echo approach adopted here allows extrapolation to TE = 0 ms to limit this source of $f_{B_1^+}$-dependent bias.

3. The approximations implemented by default in the hMRI toolbox offer flexibility but introduce $f_{B_1^+}$-dependent bias when the assumptions are violated at higher flip angle.[13] Matched TR across the SPGR acquisitions permitted T_1^{app} to be estimated without approximation[14] circumventing this potential source of bias.

At 7T, T_2 shortens increasing the feasibility of fully spoiling the transverse magnetisation. Any T_2-dependence is an important consideration since it can lead to spatially varying, microstructurally driven error in T_1 estimation. Both simulation and experiment showed that some RF spoiling increments are particularly sensitive to T_2 (Figure 5) and that the error increases in regions of high $f_{B_1^+}$. Analysis of the EPGs can provide some insights into these observations (Supporting Information S4, Supporting Information Figures S5 and S6).

However, incorporating knowledge of T_2 to correct this error is difficult since accurate quantification is challenging and time-consuming, particularly at high resolution, and can also depend on factors like $f_{B_1^+}$ and slice profiles.[46,47] Here, we have observed the T_2-dependence of T_1^{app} by measuring T_2 with a single-echo spin-echo EPI technique to maximise accuracy and minimize confounding factors. The choice of T_2 used to derive the correction factors is particularly important for the commonly used $\phi_0 = 50°$, which exhibits higher T_2 sensitivity (Figures 3, 6, and 7). Although the post-hoc correction for imperfect spoiling is not voxel-specific, global T_2 times of 35 ms *in vivo* and 60 ms in phantom, resulted in the convergence of the corrected T_1 distributions regardless of their acquisition conditions (Figures 3, 6, and 7). However, these T_2 times were smaller than literature values for *in vivo* WM at 7T[28] and those estimated with the reference protocol (T_2 of 48 ± 6 ms and 78 ± 2 ms *in vivo* and in phantom, respectively). Note that using an array of T_2 times to match those expected *in vivo* will have the same compromise effect whereby error may increase or decrease depending on the true T_2.

The issue of T_2-dependence in the estimated T_1, including after correction, has been highlighted previously at 3T.[12,19]

FIGURE 9 Numerical simulations without (BPF = 0, dashed line) and with (BPF = 0.117, solid line) a bound pool fraction leading to MT. The exchange rate from the free to the bound pool was 4.3 s^{-1},[44] and thermal equilibrium was assumed. The BPF was 0.117[44] and the diffusion coefficient was 0.8 μm^2/ms. A, T_1^{app} for ϕ_0 from 1 to 180°, T_2 = 45 ms, T_1 = 1.25 s (for both pools), and $f_{B_1^+}$ of 100%. The total dephasing per TR was set to 6π. B-C, T_1^{app} as a function of $f_{B_1^+}$ and T_2 time, respectively, for ϕ_0 = 50°, 117°, 120°, and 144°
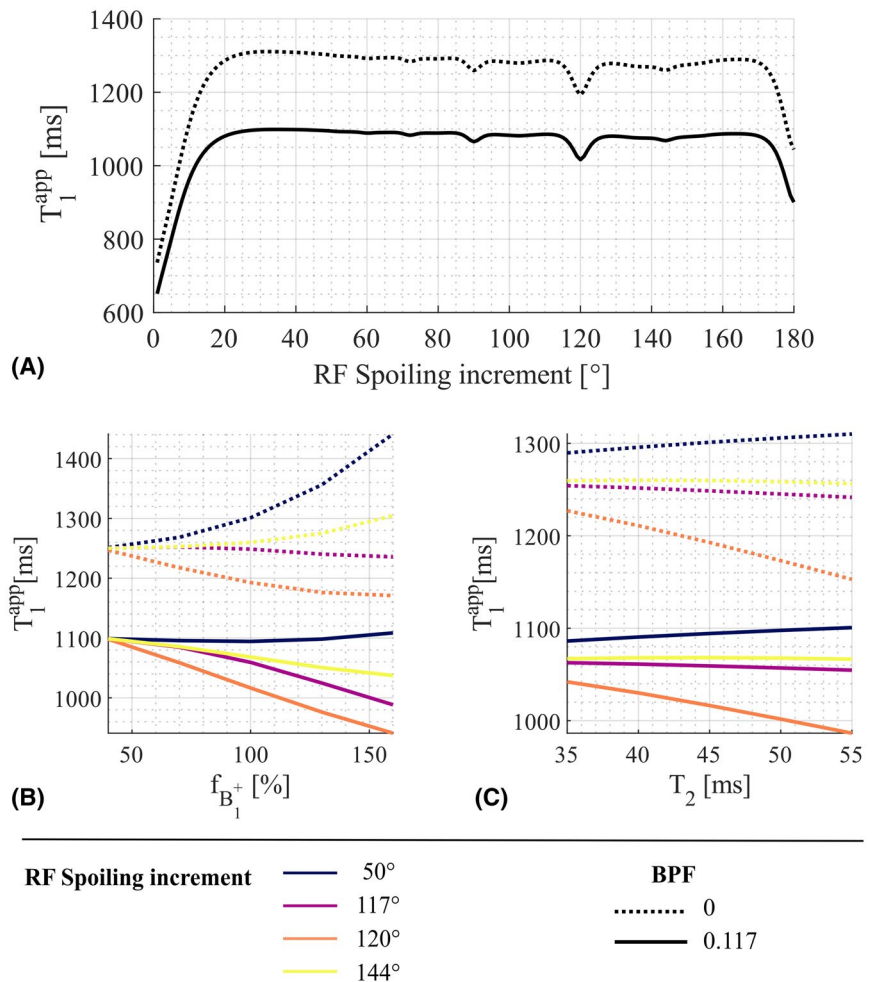
The manifestation of imperfect spoiling at 3T differs to 7T most notably by a greater dependence on the gradient spoiling and diffusional effects at 3T (see Supporting Information Figures S3 and S4 for a 3T analysis). Baudrexel et al[19] proposed an alternative correction method to the one used here, which adjusts the flip angle to account for imperfect spoiling before estimating T_1. The T_2-dependence of that technique was not compared to the method used here, but in phantoms with variable T_2, showed a residual deviation of 1 to 3%. As an alternative to estimating T_1 using an analytical solution of the Ernst equation, Heule et al[12] proposed a numerical minimization approach that does not rely on perfect spoiling. The approach performed well in comparison to the correction technique adopted here, particularly in terms of reducing theoretical sensitivity to T_2. However, the residual error increased with the diffusion coefficient and the moment of the spoiler gradient. Here, we have shown that a large spoiler moment is beneficial not only to reduce T_1^{app} sensitivities, but also to minimize artifacts due to partial voluming (Figure 8). The ghost artifacts we observed, and explained by numerical simulation, are another consequence of imperfect spoiling previously highlighted by Nielsen and Noll[31] and an important consideration when designing a protocol.

At 7T, simulations incorporating the diffusion effect, due to both the multi-echo readout and the spoiler gradient, demonstrated a detectable effect on T_1^{app} when using *in vivo* T_2 times and clinically feasible spoiler moments. In phantom, where the ADC was estimated to be 1.71 μm^2/ms, the sensitivity to $f_{B_1^+}$ depended on the spoiler gradient moment, and it was necessary to include the diffusion effect when determining the correction factors to obtain consistent T_1^{app} across φ_0, especially for the large spoiler gradient condition. In healthy *in vivo* tissue, the estimated ADC was lower (0.7 μm^2/ms) in line with literature.[29,30] The sensitivity to this parameter over the range of likely values was generally small (<1%), even for nPi = 6π, which required a net moment of 70.5 mT/m.ms at 1 mm resolution. Nonetheless, the effect of diffusion was observed *in vivo* and the T_2-dependence was reduced for ϕ_0 of 50° and 120°, when nPi was increased to 6π, in line with the simulations. Including the diffusion effect in the correction factors only had an appreciable impact with φ_0 = 120°. However, the higher the spoiler gradient moment, the higher the expected sensitivity to the diffusion coefficient (Figures 1I, Supporting Information Figures S2 and S3I).

RF spoiling increments of 50° and 117° are commonly used. 50° has the advantage of being located in a stable

region[17] but, as shown here, may not be the most suitable because of its high sensitivity to $f_{B_1^+}$ and T_2. 117° is known for being close to perfect spoiling conditions. However, it is shown here that despite reducing T_1^{app} error, residual T_2-dependence remains, especially at high $f_{B_1^+}$. $\phi_0 = 144°$ shows appealing robustness to T_2 with clinically feasible spoiler moments, making it a good candidate for VFA-based T_1 measurements. However, a broader histogram (Figure 7) and larger than predicted T_2-dependence (Figure 5E-H) were measured *in vivo* for this increment, meaning that we cannot exclude the possibility that it may be a less stable choice.[17]

4.1 | Limitations

Although efforts were made to remove confounding effects, such as anatomical variability, some discrepancies were observed between simulations and experiments (Figure 5). In addition to the issue of MT effects discussed earlier, the observed discrepancies may come from residual variance in T_1 or diffusion properties, or other microstructural features not well modeled by single pool simulations, for example, myelin water.

Some further limitations warrant discussion. This work has been performed at 7T using only a small number of protocols with many fixed parameters, for example, resolution, TR and number of echoes. Nonetheless, good agreement was observed between simulations and acquisitions indicating that the same framework could be used to investigate other protocols.

The resolution used is relatively low for 7T imaging (1 mm isotropic) but was required to maintain a tolerable scan time per session given the number of factors probed ($f_{B_1^+}$, nPi, ϕ_0). With high resolution, the diffusion effect can be expected to increase due to the larger moment of the readout gradients, while the risk of partial voluming will concurrently reduce.

The sensitivity of T_1^{app} to each of the sequence parameters and tissue properties was investigated for a limited range of values. However, these were selected to encompass the range expected in the context of neuroimaging at 7T. The sensitivity may increase in pathology, but again the validated framework presented here could be used to determine optimal protocol strategies.

5 | CONCLUSIONS

We conclude by returning to the questions posed in the introduction:

1. How do RF and gradient spoiling interact and which combination maximizes the accuracy and precision of T_1 mapping with the VFA approach?

The interaction between RF and gradient spoiling is complex. The error in T_1^{app} depends not only on ϕ_0, but also on $f_{B_1^+}$ and T_2 times, as does its sensitivity. The impact that gradient spoiling has on the error and sensitivity also depends on ϕ_0. Increasing the net gradient-induced dephasing per TR reduces the dependence on ϕ_0, except in terms of sensitivity to the diffusion coefficient (Figure 1). Since no combination achieves perfect spoiling, the preferred approach may be to maximise the robustness of T_1^{app} to other parameters that are fixed in post-hoc correction, principally T_2. Larger spoiler gradient moment has the additional benefit of improving image quality.

2. What impact does the diffusion effect have when considering clinically feasible gradient moments and the impact of the full readout?

Including the full diffusion effect of a multi-echo readout has a comparatively small impact at 7T relative to 3T for healthy tissues (Supporting Information Figures S3 and S4). Correction factors accounting for diffusion are especially important at lower field strengths due to longer T_2 or in pathology for higher diffusion coefficient, and can now be estimated via the hMRI toolbox (hmri.info[20]).

3. What are the limitations of applying simulation-derived correction factors to recover the true T_1 from T_1^{app}?

The main limitation of post-hoc correction is the need to specify a single T_2 time, leading to residual T_2-dependence. Combining $\phi_0 = 144°$ with moderate gradient spoiling minimizes the sensitivity of T_1^{app} to T_2.

ORCID
Nadège Corbin https://orcid.org/0000-0003-3296-4544
Martina F. Callaghan https://orcid.org/0000-0003-0374-1659

TWITTER
Nadège Corbin @nadege_corbin
Martina F. Callaghan @mfcallaghan

REFERENCES
1. Weiskopf N, Mohammadi S, Lutti A, Callaghan M. Advances in MRI-based computational neuroanatomy: from morphometry to in-vivo histology. *Curr Opin Neurol*. 2015;28:313-322.

2. Edwards LJ, Kirilina E, Mohammadi S, Weiskopf N. Microstructural imaging of human neocortex in vivo. *Neuroimage*. 2018;182:184-206.

3. Lutti A, Dick F, Sereno MI, Weiskopf N. Using high-resolution quantitative mapping of R1 as an index of cortical myelination. *Neuroimage*. 2014;93:176-188.

4. Sereno MI, Lutti A, Weiskopf N, Dick F. Mapping the human cortical surface by combining quantitative T1 with retinotopy. *Cereb Cortex*. 2013;23:2261-2268.

5. Carey D, Krishnan S, Callaghan MF, Sereno MI, Dick F. Functional and quantitative MRI mapping of somatomotor representations of human supralaryngeal vocal tract. *Cereb Cortex*. 2017;27:265-278.

6. Dick FK, Lehet MI, Callaghan MF, Keller TA, Sereno MI, Holt LL. Extensive tonotopic mapping across auditory cortex is recapitulated by spectrally directed attention and systematically related to cortical myeloarchitecture. *J Neurosci*. 2017;37:12187-12201.

7. Dick F, Tierney AT, Lutti A, Josephs O, Sereno MI, Weiskopf N. In vivo functional and myeloarchitectonic mapping of human primary auditory areas. *J Neurosci*. 2012;32:16095-16105.

8. Christensen K, Grant D, Schulman E, Walling C. Optimal determination of relaxation-times of Fourier-transform nuclear magnetic-resonance - determination of spin-lattice relaxation-times in chemically polarized species. *J Phys Chem*. 1974;78:1971-1977.

9. Wang H, Riederer S, Lee J. Optimizing the precision in T1 relaxation estimation using limited flip angles. *Magn Reson Med*. 1987;5:399-416.

10. Homer J, Beevers MS. Driven-equilibrium single-pulse observation of T1 relaxation. A reevaluation of a rapid "new" method for determining NMR spin-lattice relaxation times. *J Magn Reson (1969)*. 1985;63:287-297.

11. Deoni SCL, Rutt BK, Peters TM. Rapid combined T-1 and T-2 mapping using gradient recalled acquisition in the steady state. *Magn Reson Med*. 2003;49:515-526.

12. Heule R, Ganter C, Bieri O. Variable flip angle T1 mapping in the human brain with reduced t2 sensitivity using fast radiofrequency-spoiled gradient echo imaging. *Magn Reson Med*. 2016;75:1413-1422.

13. Helms G, Dathe H, Dechent P. Quantitative FLASH MRI at 3T using a rational approximation of the Ernst equation. *Magn Reson Med*. 2008;59:667-672.

14. Mohammadi S, D'Alonzo C, Ruthotto L, et al. Simultaneous adaptive smoothing of relaxometry and quantitative magnetization transfer mapping. 2017. https://doi.org/10.20347/WIAS.PREPRINT.2432

15. Ganter C. Steady state of gradient echo sequences with radiofrequency phase cycling: analytical solution, contrast enhancement with partial spoiling. *Magn Reson Med*. 2006;55:98-107.

16. Zur Y, Wood ML, Neuringer LJ. Spoiling of transverse magnetization in steady-state sequences. *Magn Reson Med*. 1991;21:251-263.

17. Preibisch C, Deichmann R. Influence of RF spoiling on the stability and accuracy of T1 mapping based on spoiled FLASH with varying flip angles. *Magn Reson Med*. 2009;61:125-135.

18. Yarnykh VL. Optimal radiofrequency and gradient spoiling for improved accuracy of T1 and B1 measurements using fast steady-state techniques. *Magn Reson Med*. 2010;63:1610-1626.

19. Baudrexel S, Nöth U, Schüre J-R, Deichmann R. T1 mapping with the variable flip angle technique: a simple correction for insufficient spoiling of transverse magnetization. *Magn Reson Med*. 2018;79:3082-3092.

20. Tabelow K, Balteau E, Ashburner J, et al. hMRI—a toolbox for quantitative MRI in neuroscience and clinical research. *Neuroimage*. 2019;194:191-210.

21. Callaghan MF, Lutti A, Ashburner J, et al. Example dataset for the hMRI toolbox. *Data Brief*. 2019;25:104132.

22. Lamy J, Loureiro de Sousa P. Sycomore: an MRI simulation toolkit. In: ISMRM. Virtual; 2020. p 2072.

23. Weigel M, Schwenk S, Kiselev VG, Scheffler K, Hennig J. Extended phase graphs with anisotropic diffusion. *J Magn Reson*. 2010;205:276-285.

24. Wright PJ, Mougin OE, Totman JJ, et al. Water proton T1 measurements in brain tissue at 7, 3, and 1.5T using IR-EPI, IR-TSE, and MPRAGE: results and optimization. *Magn Reson Mater Phy*. 2008;21:121-130.

25. Rooney WD, Johnson G, Li X, et al. Magnetic field and tissue dependencies of human brain longitudinal 1H2O relaxation in vivo. *Magn Reson Med*. 2007;57:308-318.

26. Metere R, Kober T, Möller HE, Schäfer A. Simultaneous Quantitative MRI mapping of T1, T2* and magnetic susceptibility with multi-echo MP2RAGE. *PLoS One*. 2017;12:e0169265.

27. Marques JP, Kober T, Krueger G, van der Zwaag W, Van de Moortele P-F, Gruetter R. MP2RAGE, a self bias-field corrected sequence for improved segmentation and T1-mapping at high field. *Neuroimage*. 2010;49:1271-1281.

28. Cox EF, Gowland PA. Simultaneous quantification of T2 and T′2 using a combined gradient echo-spin echo sequence at ultrahigh field. *Magn Reson Med*. 2010;64:1440-1445.

29. Helenius J, Soinne L, Perkiö J, et al. Diffusion-weighted MR imaging in normal human brains in various age groups. *Am J Neuroradiol*. 2002;23:194-199.

30. Sener RN. Diffusion MRI: apparent diffusion coefficient (ADC) values in the normal brain and a classification of brain disorders based on ADC values. *Comput Med Imaging Graph*. 2001;25:299-326.

31. Nielsen J-F, Noll DC. Improved spoiling efficiency in dynamic RF-spoiled imaging by ghost phase modulation and temporal filtering. *Magn Reson Med*. 2016;75:2388-2393.

32. Sacolick LI, Wiesinger F, Hancu I, Vogel MW. B1 Mapping by Bloch-Siegert shift. *Magn Reson Med*. 2010;63:1315-1322.

33. Hansen MS, Sørensen TS. Gadgetron: an open source framework for medical image reconstruction. *Magn Reson Med*. 2013;69:1768-1776.

34. Corbin N, Acosta-Cabronero J, Malik SJ, Callaghan MF. Robust 3D Bloch-Siegert based mapping using multi-echo general linear modeling. *Magn Reson Med*. 2019;82:2003-2015.

35. Weiskopf N, Callaghan MF, Josephs O, Lutti A, Mohammadi S. Estimating the apparent transverse relaxation time (R2*) from images with different contrasts (ESTATICS) reduces motion artifacts. *Front Neurosci*. 2014;8:278.

36. Ashburner J, Friston KJ. Unified segmentation. *Neuroimage*. 2005;26:839-851.

37. Olsson H, Andersen M, Lätt J, Wirestam R, Helms G. Reducing bias in dual flip angle T1-mapping in human brain at 7T. *Magn Reson Med*. 2020;84:1347-1358.

38. Dathe H, Helms G. Exact algebraization of the signal equation of spoiled gradient echo MRI. *Phys Med Biol*. 2010;55:4231-4245.

39. Chan K-S, Marques JP. Multi-compartment relaxometry and diffusion informed myelin water imaging – Promises and challenges of new gradient echo myelin water imaging methods. *Neuroimage*. 2020;221:117159.

40. Gras V, Abbas Z, Shah NJ. Spoiled FLASH MRI with slice selective excitation: signal equation with a correction term. *Concepts Magn Reson Part A*. 2013;42:89-100.

41. Lee Y, Callaghan MF, Nagy Z. Analysis of the precision of variable flip angle T1 mapping with emphasis on the noise propagated from RF transmit field maps. *Front Neurosci*. 2017;11:106.

42. Ou X, Gochberg DF. MT effects and T1 quantification in single-slice spoiled gradient echo imaging. *Magn Reson Med*. 2008;59:835-845.

43. Teixeira RPAG, Malik SJ, Hajnal JV. Fast quantitative MRI using controlled saturation magnetization transfer. *Magn Reson Med*. 2019;81:907-920.

44. Malik SJ, Teixeira RPAG, Hajnal JV. Extended phase graph formalism for systems with magnetization transfer and exchange. *Magn Reson Med*. 2018;80:767-779.

45. Malik S. *mriphysics/EPG-X: First public version* (Version v1.0). Zenodo. 2017. https://doi.org/10.5281/zenodo.840023

46. Noth UN, Shrestha M, Schüre SJ-R, Deichmann R. Quantitative in vivo T2 mapping using fast spin echo techniques—a linear correction procedure. *Neuroimage; Amsterdam*. 2017;157:476-485.

47. Lebel RM, Wilman AH. Transverse relaxometry with stimulated echo compensation. *Magn Reson Med*. 2010;64:1005-1014.

SUPPORTING INFORMATION

Additional Supporting Information may be found online in the Supporting Information section.

FIGURE S1 (A) Positioning of the slices used to obtain reference T_1 (B,E) and T_2 (C,F) times using single slice, single echo, spin echo EPI acquisitions. Reference ADC estimates (D,G) from the same slices are also shown. The more superior slice (yellow) had lower $f_{B_1^+}$ variance and was therefore used to investigate the T_2 dependence. The more inferior slice (red) had greater $f_{B_1^+}$ variance and was therefore used to investigate the $f_{B_1^+}$ dependence

FIGURE S2 Sensitivity of T_1^{app} to B_1^+ efficiency (A), the true T_2 time (B,C), the true T_1 time (D,E) and the diffusion coefficient (F-G) of three single-echo protocols: Protocol 1 (blue), 2 (red) and 3 (yellow). The sensitivity to T_1, T_2 and D are computed in two conditions: B_1^+ efficiency of 100% or 160%

FIGURE S3 Numerical simulations, for each spoiling condition, of T_1^{app} error in two specific cases: (A) $T_1 = 1250$ ms, D $= 0.8$ μm^2/ms, $T_2 = 65$ ms and $f_{B_1^+} = 100\%$, (B) $T_1 = 0.75$ s, D $= 1.0$ μm^2/ms, $T_2 = 55$ ms and $f_{B_1^+} = 130\%$. Sensitivity of T_1^{app} to $f_{B_1^+}$ (C), the true T_2 time (D-E), the true T_1 time (F-G) and the true diffusion coefficient (H-I). The sensitivity to T_1,

T_2 and D are computed in two conditions: B_1^+ efficiency of 100 % (D-F-H) or 130 % (E-G-I)

FIGURE S4 Acquisitions and numerical simulations at 3T for RF spoiling increments of 30°, 72°, 117°, 120° and 137°. T_1 before (ie, T_1^{app}) and after correction for imperfect spoiling with correction factors determined assuming $T_2 = 65$ ms and $D = 0.8$ μm^2/ms or ignoring diffusion. Simulations (left): true T_1 times are indicated by a solid black line at 1 s and 1.5 s. In vivo acquisitions (right): distribution of T_1 times in GM and WM where B_1^+ efficiency was between 90% and 110%

FIGURE S5 EPG diagrams, before (A, C) and after (B, D) incorporating diffusion. The diagrams depict the population amplitude of transverse, $|F_n|$ and longitudinal, $|Z_n|$, configuration states with n the degree of dephasing $\phi = 2\pi$. The simulations used a T_1 of 1000 ms, T_2 of 80 ms and a diffusion coefficient of 1.7 μm^2/s with a flip angle of 6° and a TR of 19.5 ms. Note that for visualisation purposes only a subset of the EPG diagrams are shown: $0 < n \leq 20$ for the dephasing transverse configuration states, $0 > n \geq -20$ for the rephasing transverse magnetization and $0 \leq n \leq 40$ for the longitudinal states. Higher order longitudinal and rephasing states are more populated for the RF spoiling increments of 120° and 144°. Since higher order states are especially attenuated by diffusion, incorporating this effect has the most appreciable impact on these increments. It can also be seen that sufficient pulses are incorporated to reach a steady state, which is arrived at comparatively quickly for all increments

FIGURE S6 Intra-voxel magnetisation distribution derived from the steady-state EPG coefficients for each increment (A), and the population amplitudes of the first six rephasing transverse configuration states (B). Four cases are shown: two nominal flip angles (6° and 26° corresponding to the PDw and T1w acquisitions of this study) and two T_2 times (60 ms and 80 ms). All other simulation settings are as in Supporting Information Figure S5. The net SPGR echo-forming signal (ie, F_0 state) is projected onto the transverse plane in (A) with an artificial phase dispersion added to aid visualisation